Synergy removal of Cr (VI) and organic pollutants over RP-MoS₂/rGO photocatalyst

Xue Bai[a,b], Yanyan Du[a], Xiaoyun Hu[c], Yudong He[d], Chunliang He[d], Enzhou Liu[a,e,*], Jun Fan[a,*]

[a] *School of Chemical Engineering, Northwest University, Xi'an 710069, PR China*
[b] *School of Chemistry and Chemical Engineering, Yan'an University, Yan'an 716000, PR China*
[c] *School of Physics, Northwest University, Xi'an 710069, PR China*
[d] *Xi'an Youpai Biotechnology Co., Ltd., Xi'an, 710200, PR China*
[e] *Institute of Modern Physics, Northwest University, Xi'an 710069, PR China*

A B S T R A C T

A novel RP-MoS₂/rGO nanocomposite as low-cost, environmental sustainable, stability and high-performance photocatalyst was successfully fabricated for the first time through a facile two-step hydrothermal method. Even without a noble-metal cocatalyst, the introduction of MoS₂/rGO hybrid made RP exhibit excellent photocatalytic performance, including photoreduction of Cr (VI) and photooxidation of different organic pollutants, owing to the increased number of excited electrons/holes and enhanced separation efficiency of charge carriers. Importantly, the synergy of photocatalytic reduction and oxidation, as well as photocatalysis and adsorption played an important role in enhancing photocatalytic activity and reaching a high efficiency. Besides, the chemical structure of the RP-MoS₂/rGO with P–S and P–O bands ensure the stability of the nanocomposite materials. Overall, the photocatalytic elimination of the Cr (VI)-Organic molecule coexistence system in this work shows promising application to treatment the reality wastewater.

1. Introduction

Nowadays, more and more materials as photocatalysts were exploring to deal with environmental problems, especially the excessive discharge of industrial wastewaters. Various pollutants with flowing diffusion characteristics, including organic pollutants (e.g., RhB, MB and phenol) and heavy metals (e.g., Cr (VI), Cd (II), As (V), and Hg (II)), constantly threatens the human health and sustainable development of society [1–3]. It is well-known that hexavalent chromium (Cr (VI)) is a highly dangerous metal contaminant with non-biodegradable and carcinogenic properties. For now, reduction of Cr (VI) to Cr (III) by photocatalytic technologies is regarded as one of effective methods to alleviate chromium pollution [4–7]. With the gradual improvement of photocatalytic technologies, high-efficiency, renewable and environmentally friendly photocatalysts have been investigated to remove the organic pollutants [8,9] or heavy metal [10–13], respectively. Nevertheless, only a few materials were designed to achieve the simultaneous removal of these two kinds of pollutants [14–16]. For converting solar energy into chemical energy and trying to fix the practical environmental issues, more multiple-effect photocatalysts need to be investigated to achieve the pollutants simultaneous and efficiently removal.

Red phosphorus (RP), the earth abundant elements, has been proved to perform a good photocatalytic activity with a narrow band gap around 1.4 ~ 2.0 eV [17]. Since Wang et al. [18] made the first report of RP at 2012, its inherent advantages of cheap, nontoxic and highly responsive to visible light [19,20] has been devoted to considerable attention. Yuan et al. [21] reported a hybrid photocatalyst composed by RP and g-C₃N₄ to improve the photocatalytic activity for H₂ production and CO₂ conversion. Dang et al. [22] prepared a Ni(OH)₂/P composites to alternative Pt as co-catalysts in H₂ evolution. Shi et al. [23] presented the first example of a P-CdS photocatalyst prepared by a precipitation method to enhance the photocatalytic activity. However, the study of RP-based photocatalysts is still in its infancy [24]. The morphology of red phosphorus is difficult to control and the block structure is dominant case during the previous research, which presents a poor quantum yield to restrain their practical applications. Moreover, the appropriate cocatalysts have not been extensively investigated to overcome the relatively limited light absorption performance and the high recombination probability of photogenerated electron-hole pairs. In addition, most of the RP-based investigations were applied to hydrogen generation, just a few for organics degradation [25] and no for heavy

---
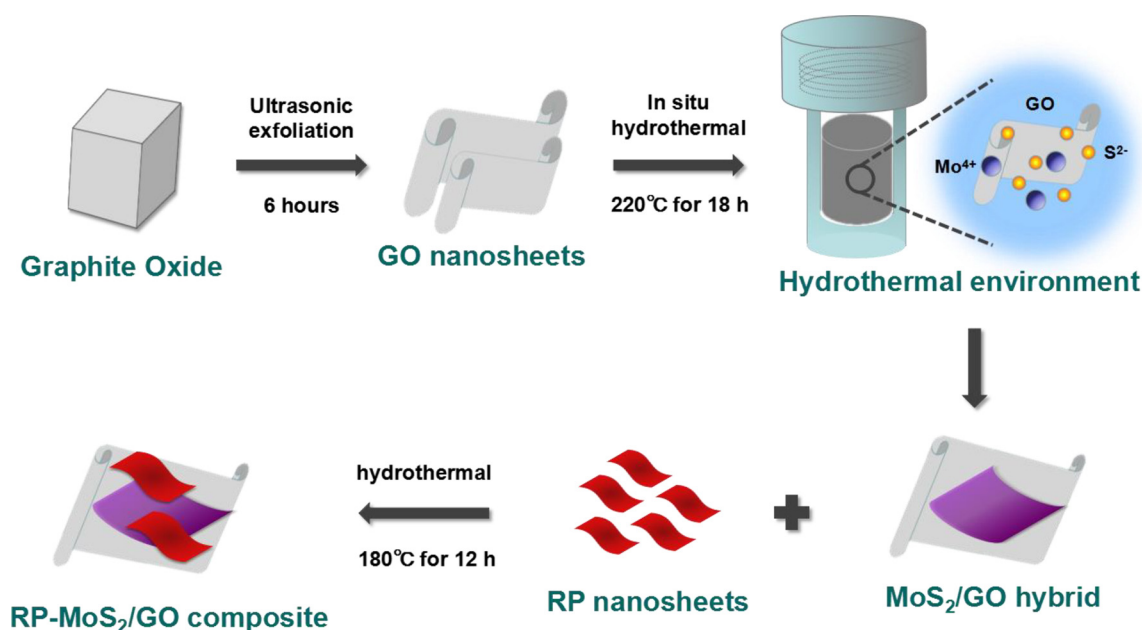
Scheme 1. Schematic illustration of the preparation of RP-MoS$_2$/rGO composite.

metals removal.

In a bid to protect the benefits gained from environmentally sustainable energy source, it is vital to find inexpensive and earth-abundant materials as cocatalyst for improving the photocatalytic performance of RP. Although Graphene Oxide (GO) and Molybdenum disulfide (MoS$_2$) alone has negligible photocatalytic activity, they are promising candidate for cocatalyst [26–28]. Except their widespread existence, both of them show extended light absorption range, enhanced charge carriers separation and transportation properties as cocatalysts to construct various semiconductor composites [29–31]. Owing to excellent electronic properties of GO, it can serve as an electron collector. Notably, the intimate interfacial contact between GO and other simiconductors has been recognized to be a key factor for sufficient utilization of electron conductivity [32–35], which have been kept in focus in our paper. Besides, GO act as a source of active adsorption sites simultaneously, due to the unique 2D structure and a large number of functional groups. Nevertheless, too much of oxygen containing groups may has a negative effect on fully contacts with other 2D materials, just like RP, which has been avoided by introducing of MoS$_2$ as presented in our paper.

Herein, we report the synthesis of RP nanosheets on a layered MoS$_2$/rGO hybrid for removal of Cr (VI) and organic pollutants simultaneously for the first time. The uniform 2D stucture was constructed by a two-step process, firstly homogeneously loading the unstacked MoS$_2$ nanosheets onto the surface of GO by in situ hydrothermal method, then coupling with RP. The introduction of P−O and P−S bonds allows intimate contacts between RP and MoS$_2$/rGO hybrid, resulting in effective charge separation and signifcantly enhanced photocatalytic activity. It is shown that the photocatalytic activity of the RP is significantly enhanced by the presence of MoS$_2$/rGO hybrid cocatalyst due to broader solar spectrum ranging and higher charge mobility. Meanwhile, the good e$^-$ transfer propertiy and adsorption of GO greatly inhibited electron-hole pairs recombination and promoted the release of photocatalytic sites of RP. To the best of our knowledge, the RP-MoS$_2$/rGO was able to achieve simultaneous reduction of Cr (VI) and oxidation of organic pollutant in a mixed state, which may boost photocatalytic removal effect in turn. Above all, the outstanding synergetic effect of simultaneous photocatalytic removal of Cr (VI) and organic pollutants with RP-MoS$_2$/rGO composite made the reaction time significantly reduced. And the essential mechanism of this study shows potentially practical application in water treatment.

2. Materials and methods

2.1. Preparation of the MoS$_2$/GO hybrid

Graphene oxide (GO) we use was prepared by the exfoliation of graphite oxide. Throughout this process, graphite oxide was homogeneously dispersed in deionized water and kept in ultraphonic treatment for 6 h. The uniform and stable slightly brown liquid was obtained and sealed reserve for use.

The MoS$_2$/GO hybrid were synthesized via in situ hydrothermal method. Ammonium molybdate and thiocarbamide were mixed into above homogeneous brown liquid in a certain mass ratio, and the mixture was well stirred, then transferred into the stainless steel autoclave with a capacity of 70 mL. Subsequently, the autoclave was sealed and maintained at 220℃ for 18 h, and then cooled down to room temperature. Finally, the samples were collected by centrifugation, washed with deionized water for several times, and dried with drying oven.

2.2. Preparation of the RP-MoS$_2$/rGO composite

A measured amount of commercial red phosphorus (Aladdin reagent corporation, AR, Purity > 98.5%, China, Shanghai) used as raw material was treated by 3 steps: 1. Milling with water and sieve out the coarse part; 2. Hydrothermal at 200℃ for 12 h, washed and centrifugal separation with deionized water repeatedly. 3. Ultrasonic for 6 h to obtain the nano-layered RP. Mix the as prepared RP and MoS$_2$/GO hybrid in deionized water, then transferr into the stainless steel autoclave at 180℃ for 12 h, after cooled down to room temperature, the samples were collected by centrifugation, washed with deionized water for several times, and dried with drying oven.

The preparation process of MoS$_2$/rGO hybrid and RP-MoS$_2$/rGO composite are shown in Scheme 1.

2.3. Characterization

The morphology and microstructure of photocatalysts were observed using scanning electron microscopy (SEM, Carl Zeiss SIGMA) and transmission electron microscopy (TEM, Tecnai G2 F20S-TWIN). The crystalline phases and chemical composition was characterized by a Shimadzu XRD-6000 powder diffractometer and Perkin-Elmer

Frontier FT-IR spectrometer with KBr pellets in the region 3000-400 cm^{-1}. X-ray photoelectron spectroscopy (XPS) was performed using a Kratos AXIS NOVA spectrometer. UV–vis diffuse reflectance spectra were obtained on a Shimadzu UV-3600 UV/vis/NIR spectrophotometer. Photoluminescence (PL) spectra were collected on a florescence spectrophotometer (Hitachi F-7000). The photoelectrochemical experiments were performed in a three-electrode system (CHI-660E, Chenhua Instruments Co., Shanghai, China). A Pt wire and saturated calomel electrode (SCE) were used as counter electrode and reference electrode, respectively. The catalyst powder was deposited on the fluoride tin oxide (FTO) substrate to serve as the working electrode. A 0.5 M Na$_2$SO$_4$ aqueous solution was employed as the electrolyte. A 300 W Xenon lamp (MICROSOLAR300UV, Beijing Perfect light) equipped with a 420 nm cutoff filter (k > 420 nm) was applied as a visible light source.

2.4. Photocatalytic activity evaluation

The photocatalytic activity of the as synthesized multiple-effect photocatalysts was performed by the simultaneous removal of Cr (VI) (prepared by using K$_2$Cr$_2$O$_7$ as the source of Cr (VI).) and RhB, Cr (VI) and MB, Cr (VI) and Phenol respectively. Xe lamp (300 W) with UV cut off filter (λ > 420 nm) as irradiation source. About 20 mg of photocatalysts was dispersed in the 50 mL of solution simultaneous containing Cr (VI) ions (40 ppm) and RhB (20 ppm), Cr (VI) ions (40 ppm) and MB (20 ppm), Cr (VI) ions (40 ppm) and Phenol (20 ppm), respectively. Prior to irradiation, the suspension was stirred in the dark for 30 min to reach the adsorption-desorption equilibrium, after which the process went on for 30 min under visible light irradiation. 3 mL of the solution was collected every 10 min, and centrifuged at a speed of 10,000 rpm to separate the photocatalyst. The clear solution were used to measure the content of Cr (VI) and RhB by UV–vis spectrometer, where the wavelength of light absorbance λ$_{max}$ of Cr (VI), RhB, MB and Phenol in solutions were at 356 nm, 554 nm, 664 nm and 270 nm.

3. Results and discussion

3.1. Characterization of RP, MoS$_2$/rGO and RP-MoS$_2$/rGO

As the charge carrier transfer processes across the interface between GO and other semiconductors has a strong impact on improving the photocatalytic efficiency. The fabrication of homogeneously dispersed MoS$_2$ onto the surface of GO and the architectural relationships among RP, MoS$_2$ and GO were illustrated in Fig. 1. From the SEM images (Fig. 1 (a–b)) we can see that prepared RP and MoS$_2$ present nanosized sheets with different morphology, and the Fig. 1 (c–d) display the similar morphology of MoS$_2$/rGO and RP-MoS$_2$/rGO, as well as their partial enlargement (Fig. 1 (e–f)), exhibiting the curly films where the GO serves as a scaffold to anchor and stabilize MoS$_2$ and RP nanosheets. Elemental mapping discloses in Fig. 1 (g) confirmed a uniform distribution of C, O, P, Mo and S throughout the RP-MoS$_2$/rGO sample. In order to distinguish the substantial differences between them, the TEM and HRTEM images of layered MoS$_2$/rGO (Fig. 1 (h–i)) and RP-MoS$_2$/rGO (Fig. 1 (j–k)) were performed. The former binary material shows that the MoS$_2$ and GO in the hybrid samples are in a very close contact, possessing unstacked layered structure. The interplanar distances of 0.615 nm and 0.227 nm correspond to the MoS$_2$ (002) and (103) planes, respectively. Obviously, the in situ growth strategy have changed the flower-like MoS$_2$ to uniform sheets and without hard aggregate on the GO film. Meanwhile GO was reduced to rGO. Throughout this process, H$_2$S released from thiocarbamide act as both the reducing agent of GO and the sulfide source. Thus, the reduction of GO and the deposition of MoS$_2$ on the rGO films occurred simultaneously, resulting in a uniform and tight distribution of MoS$_2$ nanosheets on rGO films. The same contaction happens to ternary RP-MoS$_2$/rGO samples as shown in Fig. 1 (j–k). Above exfoliated MoS$_2$/rGO with layered nanostructure was

employed as a good substrate for the growth of RP. Because of capping partial functional groups of rGO, the incorporation of RP nanosheets on MoS$_2$/rGO limits their stacking and aggregation, thereby facilitate the homogeneous coupling between them and availably kept the overall layered structure, which distinguishes the coupling occurs on RP and GO directly (as shown in Fig. S1). Moreover, TEM-EDX (energy dispersive X-ray) pattern of RP-MoS$_2$/rGO nanocomposite in Fig. S2 is in line with the chemical composition of RP-MoS$_2$/rGO and SEM-elemental mapping analyses. The EDX analysis confirmed the presence of C, O, P, Mo, and S are 12.83, 1.96, 59.26, 15.94 and 10.01 wt %, respectively, in RP-MoS$_2$/rGO nanocomposite. It can be seen that the mass ratio of RP in composite is about 60%, whose photocatalytic activity is more superior to other rations of RP. In addition, the selected-area electron diffraction (SAED) was performed to further analyse the crystallinity of the constituent nanofilms within the sample. Fig. 1 (l–n) compared the microstructural aspects and micro-constitution between RP, MoS$_2$/rGO and RP-MoS$_2$/rGO, which further confirm the construction of these nanocomposites. In good agreement with XRD results, SAED characterization (Fig. 1 (o)) of RP-MoS$_2$/rGO with scattered diffraction pattern and concentric rings reveals that the RP-MoS$_2$/rGO exhibit multi-crystal structure with nano meter level.

The functional groups present in RP, GO, MoS$_2$, MoS$_2$/rGO, and RP-MoS$_2$/rGO were identified from their FTIR spectra shown in Fig. 2a. RP spectra display absorption peaks at 1018 and 1168 cm^{-1}, which are assigned to P−O and P=O stretching vibration of phosphate [36]. The vibration bands around 1733, 1630, 1230 and 1048 cm^{-1} indicates the presence of C=O, aromatic C=C, hydroxyl C−OH and epoxy C−O−C groups respectively as a result of the functionalization of GO [37] Compared with MoS$_2$, the vibration peaks of S=O (1430, 1177 and 1038 cm^{-1}) can be observed stronger in MoS$_2$/rGO, signifying the MoS$_2$ have been loaded on the surface of GO. Besides, the absence of carbonyl and hydroxyl groups of MoS$_2$/rGO confirm that active groups on the surface of GO enables it to interact with MoS$_2$, thus can undergo surface modification. Moreover, lots of the functional groups and quite a few of defects into the aromatic structurecan of GO be removed by the in situ hydrothermal procedure at the same time. Notably, the vibrational peak of P–S bands at 665 cm^{-1} and P−O bands at 1004 and 1126 cm^{-1} [36] in the RP-MoS$_2$/rGO composites indicates that the hydrothermal process initiates the new chemical bonding between RP and MoS$_2$, RP and GO nearly at the same time. More importantly, the peaks assigned to RP becomes stronger and spectra of RP-MoS$_2$/rGO shows blue-shift, indicating the decreased imperfections and disordering of the composite structure, and the MoS$_2$/rGO hybrid as a substrate may improves the stability of RP as well.

The crystallinity and phase purity of the samples were confirmed with X-ray diffraction (XRD) as show in Fig. 2 (b). The XRD patterns of MoS$_2$ is clearly characterized to confirm the hexagonal MoS$_2$ phase corresponded to the (002), (101), (103) and (110) plane diffractions (JCPDS 87–1526), which is in accordance with the result of HRTEM image (Fig. 1 (i, k, o)). For the RP-MoS$_2$/rGO composite, all the characterized diffraction peaks of MoS$_2$ are remained, as illustrated in Fig. 2 (b), XRD patterns of MoS$_2$/rGO, RP-MoS$_2$/rGO and MoS$_2$ are basically identical, indicating that the introduction of P−S bands in RP-MoS$_2$/rGO composite does not alter the crystal lattice structure of MoS$_2$. On the other hands, the peaks of RP and GO are not detected in composite sample because of their weak crystallization. Besides, the reduction of GO could account for the disappearance of characteristic diffraction peak at around 13° [38,39].

In order to further delve the chemical composition of RP-MoS$_2$/rGO and analyse the difference of chemical states between RP-MoS$_2$/rGO composite and monomers (GO, RP and MoS$_2$), X-ray photoelectron spectroscopy (XPS) was performed and conducted as shown in Fig. 3. The full survey spectrum (Fig. 3 (a)) depicts that the composites contain the elements carbon, oxygen, phosphorus, molybdenum and sulphur, which is consistent with chemical composition of the photocatalyst. The P 2p spectrum (Fig. 3 (b)) fitted into four peaks at 130.0, 130.9, 131.4
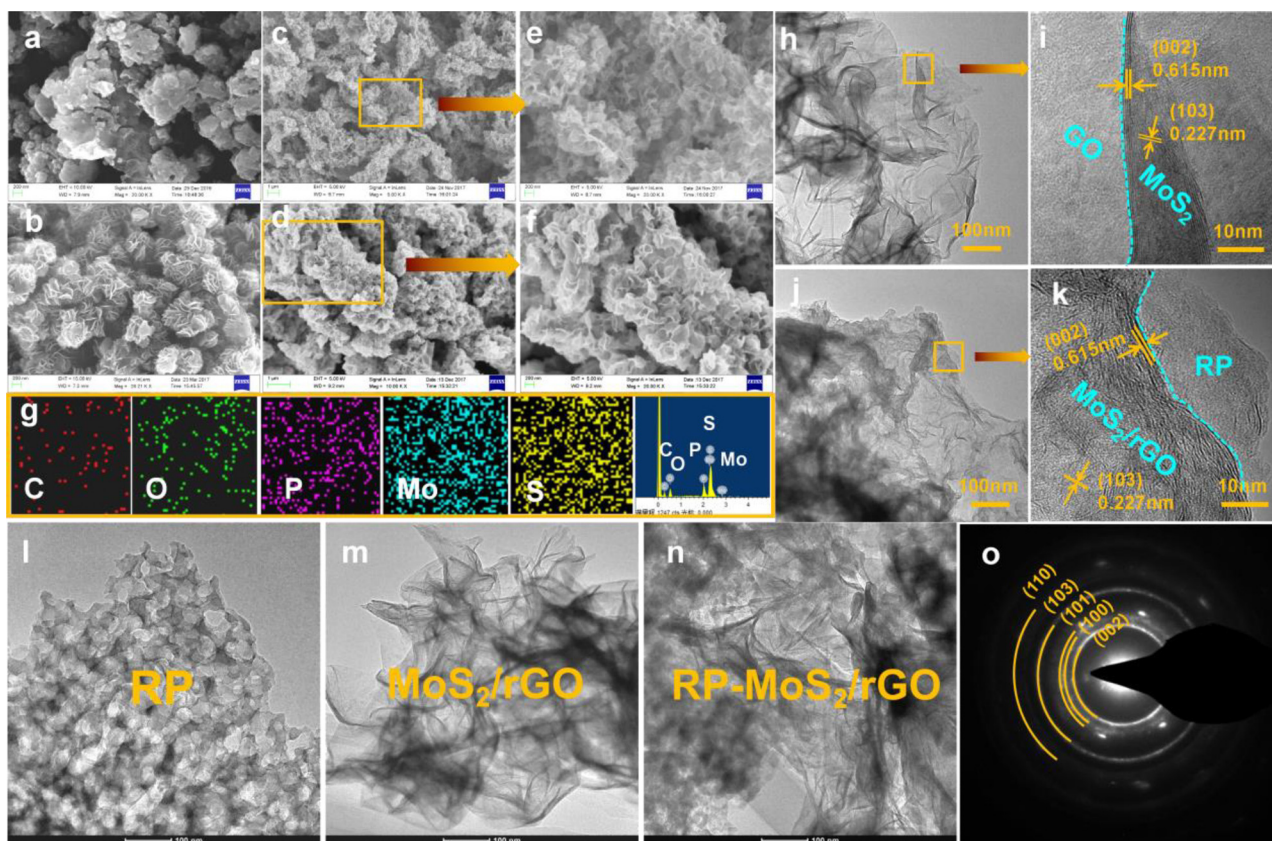
Fig. 1. (a–f) SEM images of RP, MoS$_2$, MoS$_2$/rGO and RP-MoS$_2$/rGO, (g) Elemental mapping images of C, O, P, Mo and S in plane and EDS spectrum of RP-MoS$_2$/rGO, TEM and HRTEM images of (h–i) MoS$_2$/rGO and (j–k) RP-MoS$_2$/rGO, (l–n) morphology comparasion of RP, MoS$_2$/rGO and RP-MoS$_2$/rGO and (o) SEAD pattern for RP-MoS$_2$/rGO.

and 134.6 eV are corresponding to P 2p3/2, P 2p1/2, P$_2$S$_5$ and P$_x$O$_y$, [40] respectively. Based on the above deconvoluted high resolution spectra, there are three types of P species in RP-MoS$_2$/rGO, and a new diffraction peak (P$_2$S$_5$) appeared in XPS indicating the formation of P−S bonds [41] between RP and MoS$_2$. Fig. 3 (c) presents the deconvoluted high resolution C 1 s spectrum of RP-MoS$_2$/rGO and GO, where two peaks at 284.6 eV and 285.9/286.3 eV can be attributed to C−C or C=C (graphite) and C−O. It's worth noting that, RP-MoS$_2$/rGO show stronger peak at 286.3 eV (C−O) and the peak at 287.8 eV ascribed to C=O only appeared in GO [42], manifesting that the existence of GO on the surface of RP-MoS$_2$/rGO composite is in reduction state. For RP-MoS$_2$/rGO, the binding energies of O 1 s shift to lower binding energies in

comparison with single GO, the decrease of binding energy means an increase of electron concentration [43], which further clarify the reduction of GO. Based on the high resolution Mo 3d and S 2p XPS spectra as show in Fig. 3e–f. These two spectrums of the RP-MoS$_2$/rGO are almost the same as that of and MoS$_2$, for which five main peaks were observed at the binding energies of 162.5, 163.7, 226.7, 229.7, and 232.8 eV [44], nevertheless, their peak intensities are much smaller and the binding energies shift to the lower energy compared with pure MoS$_2$, which may be attributed to the heterostructure effect between MoS$_2$ and GO & MoS$_2$ and RP. More importantly, a new diffraction peak at 162.5 eV ascribed to P$_2$S$_5$ is appeared [45], that is in good agree with above analysis of P 2p.
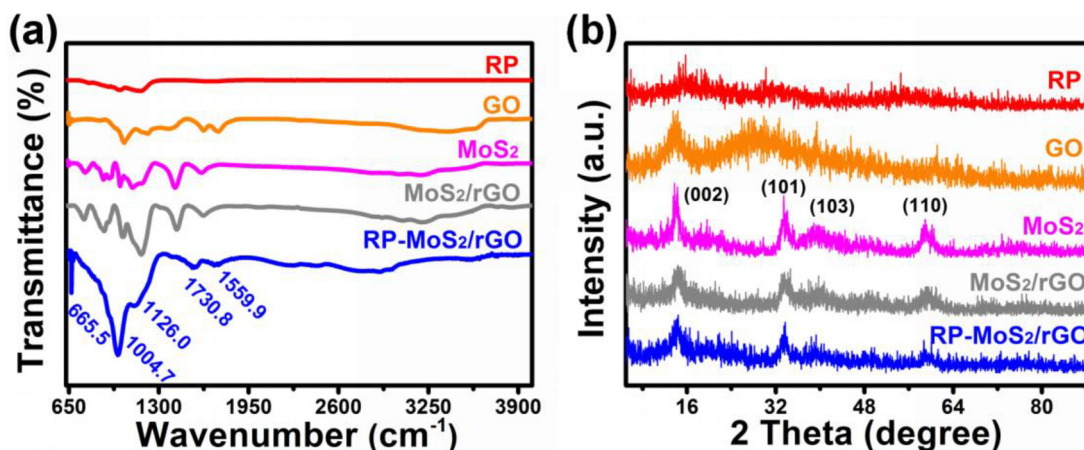
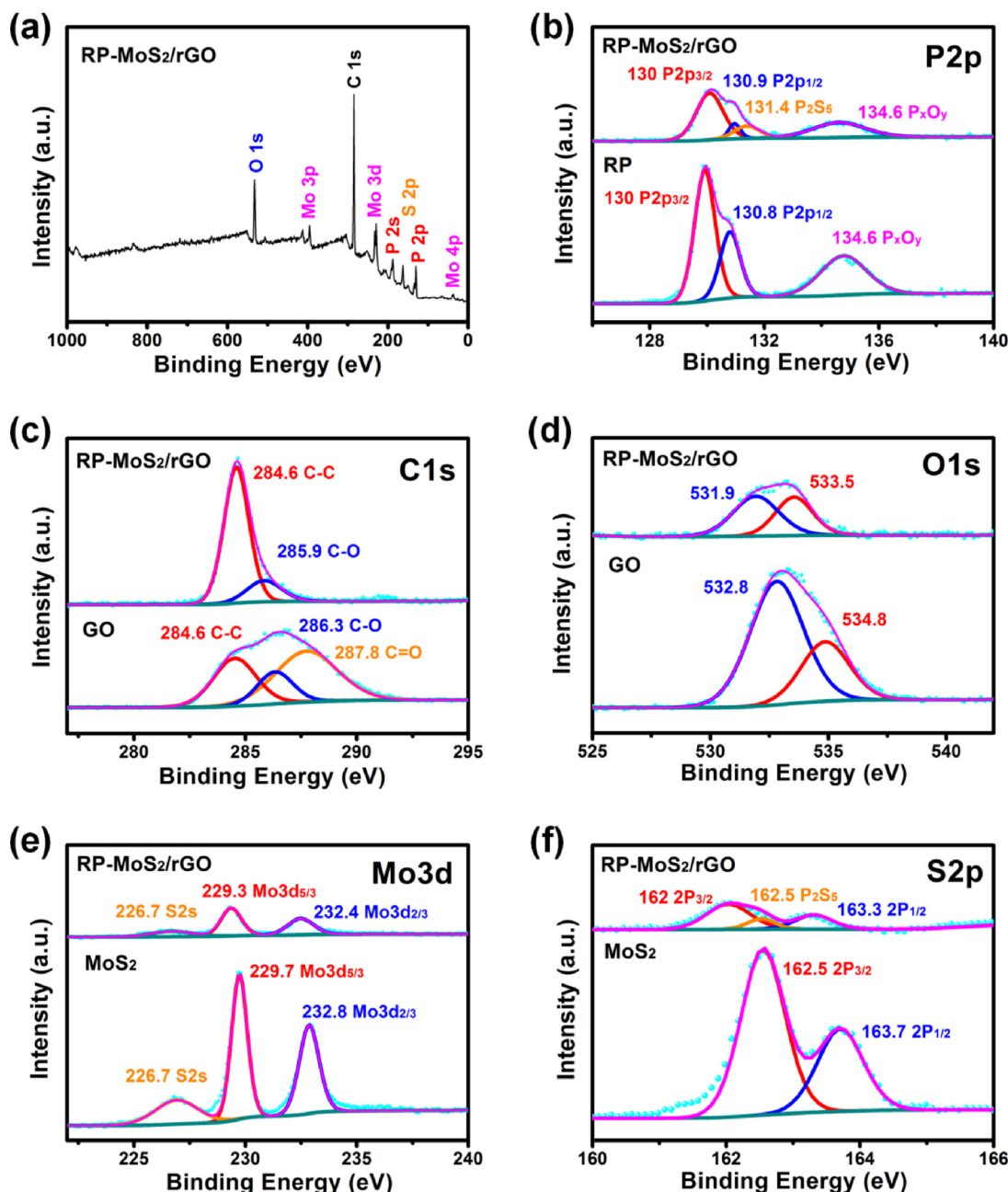**Fig. 2.** (a) FT-IR spectra and (b) XRD spectra of RP, GO, MoS$_2$, MoS$_2$/rGO, and RP-MoS$_2$/rGO.

Fig. 3. (a) Full survey XPS spectra of RP-MoS$_2$/rGO and deconvoluted high resolution spectras of (b–f) P 2p, C 1 s, O 1s, Mo 3d and S 2p in RP-MoS$_2$/rGO and monomers(GO, RP and MoS$_2$).

UV-vis absorption spectra of RP, MoS$_2$/rGO and RP-MoS$_2$/rGO composites are illustrated in Fig. 4a. The bare MoS$_2$ nanosheets show significant absorption both in the ultraviolet and visible regions. Whereas, pure RP only show a strong absorption at wavelength shorter than around 700 nm. Unsurprisingly, the RP-MoS$_2$/rGO composite possess increased optical absorption in the visible region, and show better visible-light photocatalytic performance as will be discussed later. In addition, the band gap energy (E_g) of RP and MoS$_2$ samples were calculated by: $(\alpha h\nu)^n = A(h\nu - E_g)$, where α is absorption coefficient, h is Planck's constant, ν is light frequency, E_g is band gap, A is a constant, and the value of n depends on the electronic transition of the semiconductor, of which direct-gap semiconductor and indirect-gap semiconductor are 2 and 0.5 respectively. Herein, n is 2 for RP and MoS$_2$, and the optical band gaps of these two samples were determined by using a Tauc plot with a linear extrapolation, as shown in Fig. 4b, the band gap energy of RP and MoS$_2$ are about 1.92 eV and 1.34 eV

respectively. On the above basis, the valence band (VB) and conduction band (CB) of RP and MoS$_2$ can be obtained by calculation according to the empirical formulas [46,47] :

$$E_{VB} = X - E_e + 0.5E_g$$

$$E_{CB} = E_{VB} - E_g$$

In which, X is the absolute electronegativity of the semiconductor and the X values for RP and MoS$_2$ are 5.62 and 5.32 eV, respectively. E_e is a constant knowing as energy of free electrons on the hydrogen scale (about 4.5 eV). E_g is the band gap energy of the semiconductor corresponding to RP and MoS$_2$ obtained above. Therefore, the VB and CB under the normal hydrogen electrode (NHE) are 2.07 eV and 0.17 eV for RP and 1.49 eV and 0.15 eV for MoS$_2$.
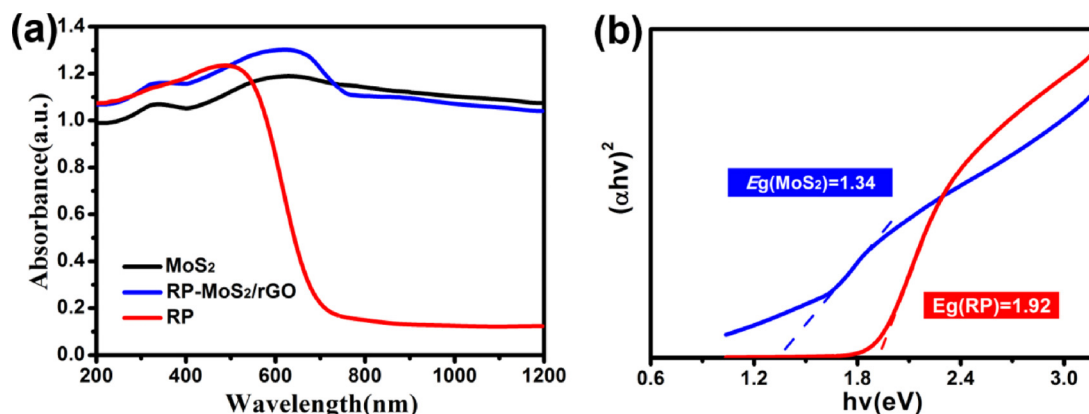
Fig. 4. (a) UV–vis DRS spectra of RP, MoS$_2$, RP-MoS$_2$/rGO and (b) Kubelka-Munk plots converted from the UV–vis DRS spectra of RP and MoS$_2$.

3.2. Simultaneous photocatalytic removal activity of materials

In this work, the simultaneous removal of solution contains 40 ppm Cr (VI) and 20 ppm RhB under visible light irradiation was carried out to evaluate the photocatalytic activities of the samples. The removal rate (X) was evaluated by $X = (C_0 - C)/C_0 \times 100\%$, where C_0 and C are the initial concentration and the concentration at time t (0–30 min) of Cr (VI) and RhB respectively. Fig.5 shown the reduction of Cr (VI) (with UV adsorption peak at 554 nm) and decolorization of RhB (with UV adsorption peak at 354 nm) by RP-MoS$_2$/rGO, RP and MoS$_2$/rGO respectivly, wherein 98.0% and 99.3% of Cr (VI) and RhB can be removed within 30 min over RP-MoS$_2$/rGO composite (Fig.5 (a–b)). However, only 58.2% and 55.9% of Cr (VI) and RhB can be removed by RP under the same constraints (Fig.5 (c–d)). MoS$_2$/GO hybrid show good adsorption performance to RhB, but the removal rate of Cr (VI) (63.4%) also much lower than RP-MoS$_2$/rGO composite (Fig.5 (e–f)). It can be found that the modification of RP shows advantage for the photocatalytic reduction of Cr (VI) and oxidation of RhB at the same time. Furthermore, The stability of the RP-MoS$_2$/rGO composite under long time photocatalytic reactions were investigated. As displayed in Fig. S3, photocatalytic reactions appeared no detrimental effects on the microstructures and elemental composition of RP-MoS$_2$/rGO composite. Moreover, the good reusability of RP-MoS$_2$/rGO photocatalysts was verified by cycling photocatalytic experiments as illustrated in Fig. S4. The results showed that RP-MoS$_2$/rGO composite possess favorable stability of both the structure and the photocatalytic performance.

It is notable that the absorption peaks of Cr(VI) and RhB are decreased obviously before irradiation. In order to confirm that the Cr(VI) was reduced by the photocatalysis, the Cr 2p XPS spectrum (Fig. S5) of photocatalyst before and after the photocatalytic reaction were investigated to indicate that the removal of Cr (VI) happens during the photocatalytic process. The dynamic adsorption of Cr(VI) and dyes (Fig. S6) were further identified that the RP-MoS$_2$/rGO composite have reached to the adsorption equilibrium before irradiation.

To investigating the photocatalytic synergy effect of the simultaneous decontamination of Cr (VI) and RhB, the visible-light photocatalytic degradation of RhB and removal of Cr (VI) were performed respectively in an isolated RhB solution (20 ppm) and an isolated Cr (VI) solution (40 ppm) for comparison. It is obvious that Cr (VI) and RhB in coexistence show superior photocatalytic activity compared with the isolated solutions as shown in Fig. 6 (a). Besides, the reactions were found to be in accordance with $-\ln(C/C_0) = K_{app}t$ (first-order kinetic equation), where K_{app} is the kinetic rate constant, C_0 is the original concentration of solution, t is the reaction time and C is the solution concentration at reaction time t. Therefore, the slope value of fitting lines shown in Fig. 6 (b) are equal to the K_{app} of RP-MoS$_2$/rGO composite for removal of Cr (VI) and RhB at different situation. Compared the K_{app} of Cr (VI) (0.071 min^{-1}) and Cr (VI) in conexistence

(0.138 min^{-1}), the latter is almost twice as many as the former. Similarly, K_{app} of RhB in conexistence (0.11 min^{-1}) is 2.62 times that of RhB (0.042 min^{-1}). All above indicating that the presence of Cr (VI) lead to an increment of photocatalytic rate, which demonstrates that Cr (VI) is an efficient scavenger of photo-generated electrons. In turn, the presence of RhB shown positive effect on Cr (VI) removal.

Above results demonstrate that RP-MoS$_2$/rGO composite performing a superior photocatalytic activity and act out a wonderful promotion through synergy of simultaneous photocatalytic decontamination of Cr (VI) and organic pollutants. Except for RhB, other organic pollutants (MB and Phenol) were utilized as target molecules for simultaneous treatment with Cr (VI), by which the photocatalytic activity of the RP-MoS$_2$/rGO composite was further determined as shown in Fig. S7. Simultaneous photocatalytic removal rates of them are summarized in Table 1. This indicates a wide variety of pollutants' decontamination over RP-MoS$_2$/rGO composite can be achieved. It is a commendable characteristic in its application on a large scale. In conclusion, the RP-MoS$_2$/rGO composite can be used as a stable photocatalyst for the removal of Cr(VI) and organic dyes. The simultaneous photocatalytic removal ability of this photocatalyst is quite impressive compared to other photocatalysts reported recently as shown in Table 2 [14–16,48–51].

3.3. Mechanism of photoreduction activity enhancement

It is clearly observed from above photocatalytic activity results that the performance of RP improved significantly when conjuncted with MoS$_2$/rGO hybrids, which manifested that MoS$_2$/rGO play a favorable role in the enhancement of photocatalytic activity of RP-MoS$_2$/rGO composites.

Firstly, MoS$_2$ can absorb full spectrum of sun light, increasing the efficiency in utilizing the visible light and near-infrared of the composites as aforementioned. On the other hand, GO serve as electron reservoir and donor in photocatalytic process could promote the separation and transportation of photogenerated carriers, as a result, enhancing the photocatalytic activity of RP-MoS$_2$/rGO. And these can be verified by analyzing the Photoluminescence (PL) spectra and electrochemical impedance spectroscopy (EIS) curves. As shown in Fig. 7 (a), PL spectra of RP, RP-GO and RP-MoS$_2$/rGO under excitation of 362 nm were displayed to study the recombination behavior of the asprepared samples. The lower PL intensity means the lower recombination of electrons and holes. Compared with pure RP, RP-GO show lower PL intensity, revealing that the added GO could hinder the recombination of charge carriers. As RP-MoS$_2$/rGO exhibit the lowest PL intensity, suggesting that the MoS$_2$/rGO may well serve as a cocatalyst for RP to minimize the charge recombination.

The EIS Nyquist plots of RP, MoS$_2$, MoS$_2$/rGO and RP-MoS$_2$/rGO were presented in Fig. 7 (b) to provide the evidence of the faster
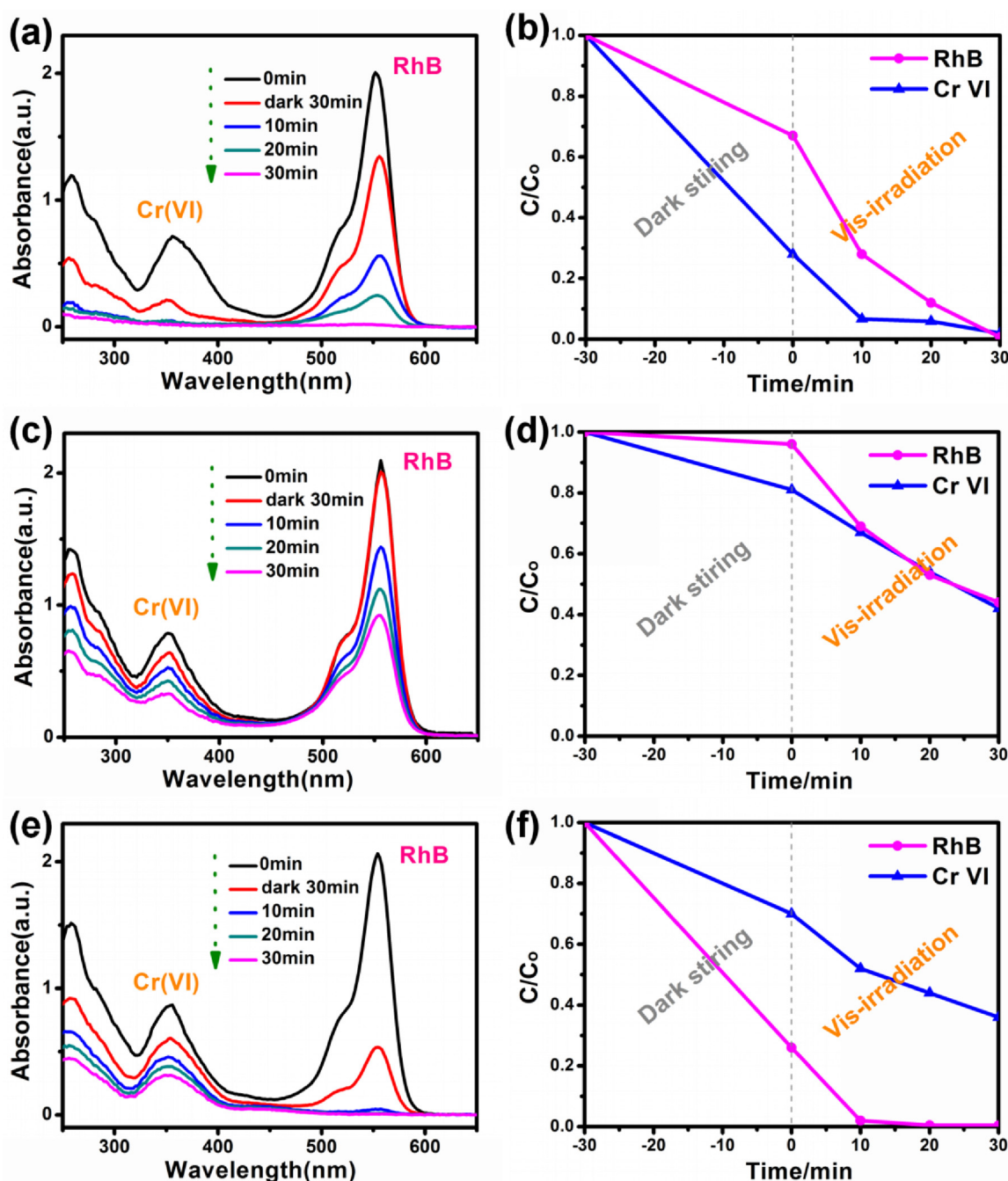
Fig. 5. Comparison of photocatalytic activity of (a, b) RP-MoS$_2$/rGO, (c, d) RP and. (e, f) MoS$_2$/rGO under visible light irradiation.

transportation of photoexcited electrons of these samples. Generally speaking, a higher mobility and separation of photoexcited electron-hole pairs will result in a smaller arc radius. It is obvious that the arc radius decreases with the introducing of MoS$_2$/rGO, which causes a remarkable decrease in the radius of the arc compared with the pure RP. All above indicated that using MoS$_2$/rGO as cocatalyst may accelerate the interfacial charges transfer and suppresses the charge re-combination, which is beneficial to photocatalysis.

As we mentioned above, the band gap energy of RP and MoS$_2$ are about 1.92 eV and 1.34 eV and the VB and CB under the NHE are 2.07 eV and 0.17 eV for RP and 1.49 eV and 0.15 eV for MoS$_2$. To our knowledge, reduction of Cr (VI) may attribute to photoinduced elec-trons (e$^-$) in the CB. While, the reactive oxygen species involved in the photocatalytic oxidation process are quite a lot, such as $\cdot O_2^-$, h$^+$ and $\cdot$

OH [52,53]. To approach to the oxidation mechanism, we confirmed the active oxidation species for organic pollutants by contrasting the band structures of RP-MoS$_2$/rGO photocatalyst and the electromotive force of $\cdot O_2^-$. and $\cdot$OH. As shown in Scheme 2, $\cdot O_2^-$ (E$_o$(O$_2$/$\cdot O_2^-$) = −0.33 eV) [54] and $\cdot$OH (E$_o$($^-$OH/$\cdot$OH) = 2.38 eV) [55] are unable to obtain from O$_2$ and H$_2$O. Therefore, e$^-$ and h$^+$ were used to involved in the REDOX reaction directly during this work. Besides, we further test the effect of these reactive species on the photocatalytic oxidation, as the scavengers of $\cdot O_2^-$, h$^+$ and $\cdot$OH, benzoquinone (BQ), ammo-nium oxalate (AO) and Isopropanol (IPA) were added to the reaction system. From Fig. S8, BQ and IPA show little effect on the RhB de-gradation, which indicates that $\cdot O_2^-$ and $\cdot$OH are not the main reactive species in the photocatalytic oxidation process. However, upon the addition of AO, the efficiency decreased seriously, suggesting that h$^+$ is
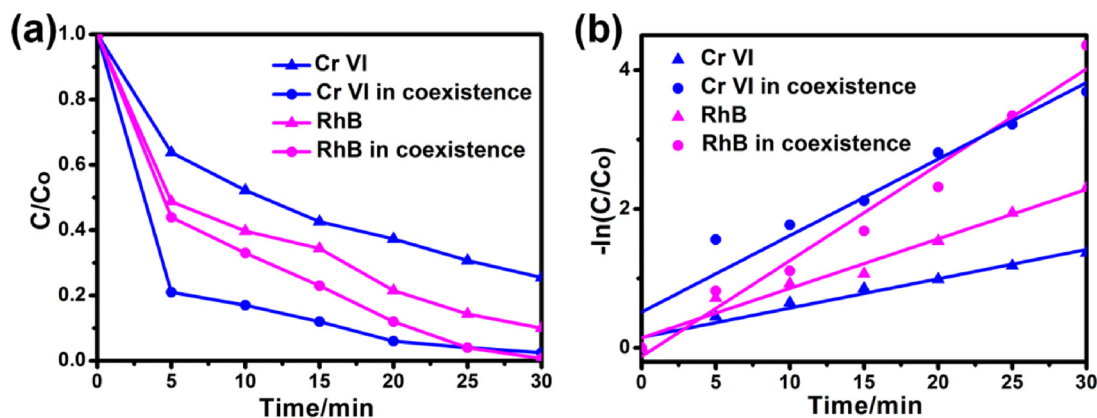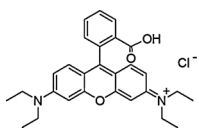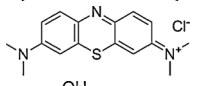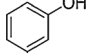
Fig. 6. (a) Photoreduction of Cr(VI) and photooxidation of RhB by RP-MoS$_2$/rGO with different situation; (b) The corresponding fitted reaction kinetic curves (-ln(C/C$_o$) = kt).

Table 1
Simultaneous photocatalytic removal rates of Cr (VI) and organic pollutants.

Organic pollutants	Molecular formula	Constitutional formula	Simultaneous photocatalytic removal rate (X)
Rhodamine B (RhB)	$C_{28}H_{31}ClN_2O_3$		$X_{Cr(VI)} = 98.0\%$ $X_{RhB} = 99.3\%$
methylene blue (MB)	$C_{16}H_{18}ClN_3S$		$X_{Cr(VI)} = 89.7\%$ $X_{MB} = 96.9\%$
Phenol	C_6H_5OH		$X_{Cr(VI)} = 98.7\%$ $X_{Phenol} = 99.1\%$

The photocatalytic removal rate of different organic pollutants and photocatalysts are highlighted in bold to exaggerate the contrast, which are the core contents in tables.

the main reactive species in the photocatalytic oxidation process. Moreover, scavengers show no effect on the Cr (VI) reduction at the same time.

Based on the above analyses, the possible photocatalytic mechanism of the RP-MoS$_2$/rGO has been demonstrated for the better understanding of the photocatalytic simultaneous decontamination process, in which the photocatalytic performance of RP-MoS$_2$/rGO photocatalyst only related to the quantity and activity of e$^-$ and h$^+$. Moreover, GO displayed an important role in storing, shuttling electrons and good adsorption. Importantly, Cr (VI) and organic pollutants serve as scavenger for each other may consume e$^-$ and h$^+$ concurrently, resulting in the synergy effect between reduction of Cr (VI) and the oxidation of organic pollutants. On the other hand, this synergy effect may perform a significantly benificial to suppress the recombination of carriers and facilitate the photocatalytic reaction, overall assists in enhancing photocatalytic activity.

4. Conclusions

The proposed method for simultaneous removal of Cr (VI) and organic pollutions with RP-MoS$_2$/rGO was very promising due to significant synergy of photocatalytic redox reactions. The flat carbon of
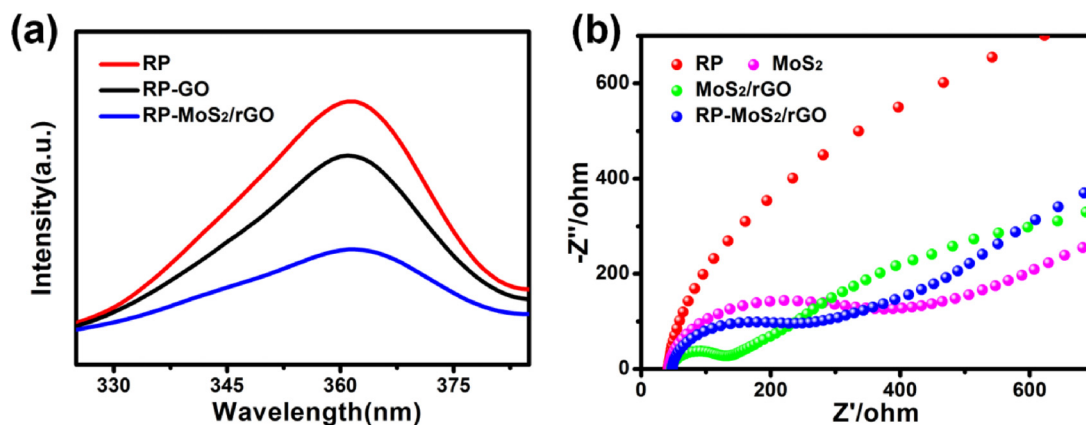
Table 2
Comparison of simutaneous photocatalytic removal rate between different materials.

Photocatalysts/ Amount (mg)	Journals/ Publication date	Solutions / Volume (mL)/concentration (ppm)	Time (min)	Photocatalytic removal rate	Ref.
RP-MoS$_2$/rGO/ 20	Applied Catalysis B: Environmental	Cr(VI)/ 50/ 40	30	**98.0**	This study
		RhB/ 50/ 20		**99.3**	
		Cr(VI)/ 50/ 40		**89.7**	
		MB/ 50/ 20		**96.9**	
		Cr(VI)/ 50/ 40		**98.7**	
		Phenol/ 50/ 20		**99.1**	
TiO$_2$-based nanorods-g-C$_3$N$_4$(TNRs-C$_3$N$_4$)/	Nanoscale/ 2017	Cr(VI)/ 200/ 40	70	**94.7**	[14]
		RhB/ 200/ 20		**98.9**	
2D MoS$_2$/RP/ 50	Materials Letters/ 2018	Cr(VI)/ 100/ 40	80	**72.7**	[15]
		RhB/ 100/ 10		**97.5**	
(Fe˚) doped g-C$_3$N$_4$/MoS$_2$/ 30	ACS Sustainable Chemistry & Engineering/ 2016	Cr(VI)/ 50/ 20	120	**98.2**	[16]
		RhB/ 50/ 20		**91.4**	
BiOI/rGO/Bi$_2$S$_3$/ 50	Chemosphere/ 2017	Cr(VI)/ 50/ 50	240	**70**	[48]
		Phenol/ 50/ 10		**95**	
Cu nanoparticles sensitized TiO$_2$ nanotube arrays	Applied Surface Science/ 2016	Cr(VI)/20/10	120	**45.0**	[49]
		RhB/ 50/ 20		**95.7**	
CdS QDs-Doped γ-Bi$_2$MoO$_6$/ 20	ACS Omega/ 2017	Cr(VI)/20/100	60	**97**	[50]
		Phenol/ 20/ 10		**47**	
Ag@Ag$_3$PO$_4$/g-C$_3$N$_4$/ NiFe LDH/ 20	ACS Omega/ 2018	Cr(VI)/20/20	120	**97**	[51]
		Phenol/ 20/20		**90**	

The photocatalytic removal rate of different organic pollutants and photocatalysts are highlighted in bold to exaggerate the contrast, which are the core contents in tables.
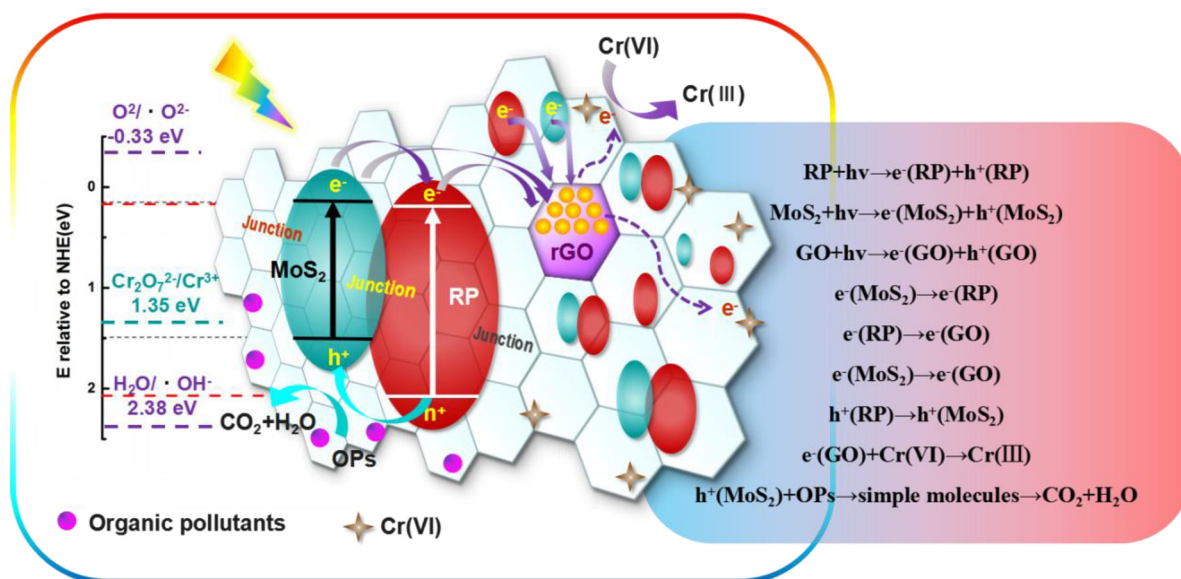
Fig. 7. (a) PL spectra of RP, RP-GO, RP-MoS$_2$/rGO and (b) EIS spectra of RP, MoS$_2$, MoS$_2$/rGO and RP-MoS$_2$/rGO.

Scheme 2. Schematic illustration of photocatalytic removal mechanism of Cr(VI) and organic pollutants over RP-MoS$_2$/rGO composite.

GO was served as a scaffold to anchor MoS$_2$, and obtained MoS$_2$/rGO hybrid was fabricated to stabilize and improve the dispersibility of RP. Moreover, above obtained appropriate nanostructure of RP-MoS$_2$/rGO photocatalyst present a good adsorption ability, which can assist in promoting selectivity and efficiency of the catalytic process. Furthermore, MoS$_2$/rGO hybrid possess better visible-light photocatalytic performance and significantly improve the effective charge transformation of RP, which directly enhance the photocatalytic activity. Overall, the application of the RP-MoS$_2$/rGO to the removal of the Cr (VI)-Organic molecule coexistence system is quite impressive, and the mechanism of multiple-effect photocatalytic process was given to show a promising path to treatment the reality wastewater.

Acknowledgments

Appendix A. Supplementary data

Supplementary material related to this article can be found, in the online version, at doi:https://doi.org/10.1016/j.apcatb.2018.08.016.

References

[1] Y. Zhao, C. Eley, J. Hu, Angew. Chem. 51 (2012) 3846–3849.
[2] Z. Yu, B. Yin, F. Qu, X. Wu, Chem. Eng. 258 (2014) 203–209.
[3] S. Xu, S. Pan, Y. Xu, Y. Luo, Y. Zhang, G. Li, J. Hazard. Mater. 283 (2015) 7–13.
[4] G. Chen, M. Sun, Q. Wei, Z. Ma, B. Du, Appl. Catal. B-Environ. 125 (2012) 282–287.
[5] L. Wang, X. Li, W. Teng, Q. Zhao, Y. Shi, R. Yue, Y. Chen, J. Hazard. Mater. 244-245 (2013) 681–688.
[6] X. Meng, X. Zhang, N. Li, Chem. Eng. J. 314 (2017) 249–256.
[7] S. Fang, Y. Zhoua, M. Zhou, Zh Li, S. Xu, C. Yao, J. Ind. Eng. Chem. 58 (2018) 64–73.
[8] E. Pajootan, M. Rahimdokht, M. Arami, J. Ind. Eng. Chem. 55 (2017) 149–163.
[9] Y. Hao, X. Dong, S. Zhai, X. Wang, H. Ma, X. Zhang, Chem. Commun. (Camb.) 52 (2016) 6525–6528.
[10] J. Wan, X. Du, E. Liu, Y. Hu, J. Fan, X. Hu, J. Catal. 345 (2017) 281–294.
[11] S. Park, R. Selvaraj, M.A. Meetani, Y. Kim, J. Ind. Eng. Chem. 45 (2017) 206–214.
[12] Y. Yao, Y. Hu, M. Yu, C. Lian, M. Gao, J. Zhang, G. Li, S. Wang, Chem. Eng. J. 344 (2018) 535–544.
[13] Y. Yao, J. Zhang, H. Chen, M. Yu, M. Gao, Y. Hu, S. Wang, Appl. Surf. Sci. 440 (2018) 421–431.
[14] D. Lu, P. Fang, W. Wu, J. Ding, L. Jiang, X. Zhao, C. Li, M. Yang, Y. Li, D. Wang, Nanoscale 9 (2017) 3231–3245.
[15] X. Bai, J. Wan, J. Jia, X. Hu, Y. He, C. He, E. Liu, J. Fan, Mater. Lett. 222 (2018) 187–191.
[16] X. Wang, M. Hong, F. Zhang, Z. Zhuang, Y. Yu, ACS Sustain. Chem. Eng. 4 (2016) 4055–4063.
[17] S.A. Ansari, Z. Khan, M.O. Ansari, M.H. Cho, RSC Adv. 6 (2016) 44616–44629.
[18] F. Wang, W. Ng, J. Yu, H. Zhu, C. Li, L. Zhang, Z. Liu, Q. Li, Appl. Catal. B-Environ. 111-112 (2012) 409–414.

[19] Y. Fujita, H.O. Venterink, P.M. van Bodegom, J.C. Douma, G.W. Heil, N. Hölzel, E. Jabłońska, W. Kotowski, T. Okruszko, P. Pawlikowski, P.C. de Ruiter, M.J. Wassen, Nature 505 (2014) 82–86.

[20] B.C. Koo, Y.H. Lee, D.S. Moon, S.C. Yoon, J.C. Raymond, Science 342 (2013) 1346–1348.

[21] Y.P. Yuan, S.W. Cao, Y.S. Liao, L.S. Yin, C. Xue, Appl. Catal. B-Environ. 140-141 (2013) 164–168.

[22] H. Dang, X. Dong, Y. Dong, H. Fan, Y. Qiu, RSC Adv. 4 (2014) 44823–44826.

[23] Z. Shi, X. Dong, H. Dang, Int. J. Hydrogen Energy 41 (2016) 5908–5915.

[24] Z. Hu, Z. Shen, J. Yu, Green Chem. 19 (2017) 588.

[25] W. Li, Y. Zhang, G. Tian, S. Xie, Q. Xu, L. Wang, J. Tian, Y. Bu, J. Mol. Catal. A-Chem. 423 (2016) 356–364.

[26] Q. Xiang, J. Yu, M. Jaroniec, J. Am. Chem. Soc. 134 (2012) 6575–6578.

[27] K. Chang, Z. Mei, T. Wang, Q. Kang, S. Ouyang, J. Ye, ACS Nano 8 (2014) 7078–7087.

[28] X. Zong, H. Yan, G. Wu, G. Ma, F. Wen, L. Wang, C. Li, J. Am. Chem. Soc. 130 (2008) 7176–7177.

[29] Q. Xiang, J. Yu, M. Jaroniec, Soc. Rev. 41 (2012) 782–796.

[30] S. Chowdhury, R. Balasubramanian, Appl. Catal. B-Environ. 160-161 (2014) 307–324.

[31] Y. Liu, H. Zhang, J. Ke, J. Zhang, W. Tian, X. Xu, X. Duan, H. Sun, M. Tade, S. Wang, Appl. Catal. B-Environ. 228 (2018) 64–74.

[32] Y. Yuan, Z. Ye, H. Lu, B. Hu, Y. Li, D. Chen, J. Zhong, Z. Yu, Z. Zou, ACS Catal. 6 (2016) 532–541.

[33] J. Zhang, Q. Wang, L. Wang, X. Li, W. Huang, Nanoscale 7 (2015) 10391–10397.

[34] J. Low, S. Cao, J. Yu, S. Wageh, Chem. Commun. (Camb.) 50 (2014) 10768–10777.

[35] K. Cho, K. Kim, H. Choi, H. Jung, Green Chem. 17 (2015) 3972–3978.

[36] Y. Zhao and X. Sun, The Science Publishing Company, China, 2003.

[37] T. Kuila, S. Bose, P. Khanra, A.K. Mishra, N.H. Kim, J.H. Lee, Carbon 50 (2012) 914.

[38] Z. Fan, K. Wang, T. Wei, J. Yan, L. Song, B. Shao, Carbon 48 (2010) 1670–1692.

[39] Y. Li, W. Cui, L. Liu, R. Zong, W. Yao, Y. Liang, Y. Zhu, Appl. Catal. B-Environ. 199 (2016) 412–423.

[40] X. Zhang, H. Xie, Z. Liu, C. Tan, Z. Luo, H. Li, J. Lin, L. Sun, W. Chen, Z. Xu, L. Xie, W. Huang, H. Zhang, Angew. Chem. Int. Ed. 54 (2015) 3653–3657.

[41] N. Tanibata, H. Tsukasaki, M. Deguchi, S. Mori, A. Hayashi, M. Tatsumisago, J. Mater. Chem. A Mater. Energy Sustain. 5 (2017) 11224–11228.

[42] S. Stankovich, R. Piner, X. Chen, N. Wu, S. Nguyen, R. Ruoff, J. Mater. Chem. 16 (2005) 155–158.

[43] Z. Zhang, K. Liu, Z. Feng, Y. Bao, B. Dong, Sci. Rep. 6 (2016) 19221.

[44] C. Liu, L. Wang, Y. Tang, S. Luo, Y. Liu, S. Zhang, Y. Zeng, Y. Xu, Appl. Catal. B-Environ. 164 (2015) 1–9.

[45] T. Matsuyama, M. Deguchi, K. Mitsuhara, T. Ohta, T. Mori, Y. Orikasa, Y. Uchimoto, Y. Kowada, A. Hayashi, M. Tatsumisago, J. Power Sour. 313 (2016) 104–111.

[46] Y. Li, S. Wu, L. Huang, H. Xu, R. Zhang, M. Qu, Q. Gao, H. Li, J. Phys. Chem. Solids 76 (2015) 112–119.

[47] Y. Hong, Y. Jiang, C. Li, W. Fan, X. Yan, M. Yan, W. Shi, Appl. Catal. B-Environ. 180 (2016) 663–673.

[48] A. Chen, Z. Bian, J. Xu, X. Xin, H. Wang, Chemosphere 188 (2017) 659–666.

[49] J. Zhong, Q. Wang, J. Zhou, D. Chen, Z. Ji, Appl. Surf. Sci. 367 (2016) 342–346.

[50] D. Kandi, S. Martha, A. Thirumurugan, K.M. Parida, ACS Omega 2 (2017) 9040–9056.

[51] S. Nayak, K.M. Parida, ACS Omega 3 (2018) 7324–7343.

[52] X. Zhou, C. Hu, X. Hu, T. Peng, J. Qu, J. Phys. Chem. C 114 (2010) 2746–2750.

[53] Y. Yang, G. Zhang, S. Yu, X. Sheng, Chem. Eng. J. 162 (2010) 171–177.

[54] J. Kim, C.W. Lee, W. Choi, Environ. Sci. Technol. 44 (2010) 6849–6854.

[55] H. Cheng, B. Huang, Y. Dai, X. Qin, X. Zhang, Langmuir 26 (2010) 6618–6624.